

PAPER • OPEN ACCESS

Correlative spatter and vapour depression dynamics during laser powder bed fusion of an Al-Fe-Zr alloy

To cite this article: Da Guo *et al* 2024 *Int. J. Extrem. Manuf.* **6** 055601

View the [article online](#) for updates and enhancements.

You may also like

- [Hybrid modeling and optimization of fiber laser hole cutting of austenitic stainless-steel sheets using response surface](#)
Zhenhua Niu, Mohammad Hossein Razavi Dehkordi, Mohammadreza Ghazi *et al.*
- [Effect of magnetic field frequency on the shape of GMAW welding arc and weld microstructure properties](#)
Zi Qi Guan, Hong Xu Zhang, Xiao Guang Liu *et al.*
- [Experimental and numerical study of spatter formation and composition change in fiber laser welding of aluminum alloy](#)
Dongsheng Wu, Xueming Hua, Youxiong Ye *et al.*

Correlative spatter and vapour depression dynamics during laser powder bed fusion of an Al-Fe-Zr alloy

Da Guo^{1,2} , Rubén Lambert-García^{1,2}, Samy Hocine^{1,2}, Xianqiang Fan^{1,2}, Henry Greenhalgh³, Ravi Shahani⁴, Marta Majkut⁵, Alexander Rack⁵ , Peter D Lee^{1,2,*}  and Chu Lun Alex Leung^{1,2,*} 

¹ UCL Mechanical Engineering, University College London, London WC1E 7JE, United Kingdom

² Research Complex at Harwell, Harwell Campus, Didcot OX11 0FA, United Kingdom

³ HiETA Technologies, Bristol BS16 7FR, United Kingdom

⁴ Constellium Technology Centre, 38341 Voreppe, France

⁵ ESRF—The European Synchrotron, 38000 Grenoble, France

E-mail: peter.lee@ucl.ac.uk and alex.leung@ucl.ac.uk

Received 31 January 2024, revised 16 April 2024

Accepted for publication 19 May 2024

Published 5 June 2024



CrossMark

Abstract

Spatter during laser powder bed fusion (LPBF) can induce surface defects, impacting the fatigue performance of the fabricated components. Here, we reveal and explain the links between vapour depression shape and spatter dynamics during LPBF of an Al-Fe-Zr aluminium alloy using high-speed synchrotron x-ray imaging. We quantify the number, trajectory angle, velocity, and kinetic energy of the spatter as a function of vapour depression zone/keyhole morphology under industry-relevant processing conditions. The depression zone/keyhole morphology was found to influence the spatter ejection angle in keyhole versus conduction melting modes: (i) the vapour-pressure driven plume in conduction mode with a quasi-semi-circular depression zone leads to backward spatter whereas; and (ii) the keyhole rear wall redirects the gas/vapour flow to cause vertical spatter ejection and rear rim droplet spatter. Increasing the opening of the keyhole or vapour depression zone can reduce entrainment of solid spatter. We discover a spatter-induced cavity mechanism in which small spatter particles are accelerated towards the powder bed after laser-spatter interaction, inducing powder denudation and cavities on the printed surface. By quantifying these laser-spatter interactions, we suggest a printing strategy for minimising defects and improving the surface quality of LPBF parts.

Supplementary material for this article is available [online](#)

Keywords: spatter, vapour depression, x-ray imaging, defects, surface quality

* Authors to whom any correspondence should be addressed.



Original content from this work may be used under the terms of the [Creative Commons Attribution 4.0 licence](#). Any further distribution of this work must maintain attribution to the author(s) and the title of the work, journal citation and DOI.

1. Introduction

Laser powder bed fusion (LPBF) is a prominent additive manufacturing (AM) technology that manufactures near-net shape metallic components with exceptional design freedom, minimal lead time, and no tooling cost, on a layer-by-layer basis [1–4]. However, the adoption of LPBF for safety critical applications is hindered by the challenge of achieving defect-free, high-density metallic components that meet critical quality standards [5, 6].

High-quality LPBF components can be superior to castings in defect levels and mechanical properties when appropriate process parameters are used [7]; however, currently they may not reach the surface quality and defect levels of components machined from wrought products. Aluminium LPBF is currently an attractive solution for the replacement of machined components only in a few niche applications, as machining of aluminium is relatively inexpensive for large numbers and waste can be recycled efficiently. Industrial adoption of aluminium LPBF becomes attractive for production of short lead time prototypes such as spare parts with non-machined surfaces, or for replacing complex systems of component assemblies with a single AM component [8, 9].

Casting alloys such as AlSi10Mg [10] and high-strength alloys, e.g. 6xxx and 7xxx series [11], may suffer from poor mechanical performance or poor processability in AM applications. To achieve superior properties (strength and conductivity) with good LPBF processability, Constellium Ahead® CP1 aluminium was designed specifically for LPBF based on the Al-Fe-Zr rapid solidification alloy system and registered with the Aluminium Association as AA8A61.50 [12]. The alloy design simplifies LPBF production. After printing, a precipitation hardening treatment, typically at 400 °C for 4 h, is used to reach a peak yield strength of ~300 MPa and high levels of thermal ($180 \text{ W}\cdot\text{m}^{-1}\cdot\text{K}^{-1}$) and electrical (up to $30 \text{ mS}\cdot\text{m}^{-1}$) conductivity [13]. The printed components of AA8A61.50 usually show high intrinsic defect tolerance and low residual stress, resulting in excellent fatigue performance even on non-machined samples with printing flaws. Reduced defects (or roughness) in the surface regions should bring further improvements on the fatigue performance of the LPBF components. These surface defects are often associated with spatter formation [1, 14–19] during LPBF and hence a better understanding of their evolution mechanisms is required to prevent them.

Four types of ejecta have been found in LPBF processes based on their formation mechanisms: (i) solid spatter, (ii) entrainment spatter, (iii) powder agglomeration, and (iv) liquid droplet spatter [20]. Solid spatter forms when powder particles are directly ejected by the high-pressure metallic vapour plume at the laser-matter interaction zone [16, 21]. Entrainment spatter occurs when particles are entrained by a combination of inward shielding gas flow induced by the high-speed vapour plume and the wakefield generated by the scanning laser beam [22]. Powder agglomeration occurs when powder particles exhibit modified surface chemistry and a high cohesion index

owing to the presence of adventitious carbon, moisture, oxidation, or partial sintering [23]. Liquid droplets mainly form from the front wall of the turbulent melt pool due to the vapour-induced recoil pressure (P_r) [22, 24].

Liquid droplet and powder agglomeration spatter, usually exhibit a larger particle size than the feedstock, and are frequently identified as a major type of defect during LPBF [25]. Oversized spatter can adhere to the surface of AM parts, increasing both surface defects and roughness [15]; they can also be trapped in the powder bed in subsequent build layers, leading to lack-of-fusion porosities [26]. Spatter may undergo oxidation [27], which lowers the recyclability and reusability of powder [28]. The surface oxides can inhibit particle fusion and promote the formation of porosity [23], decreasing the density of the LPBF parts. However, the role of small spatter on the final product properties remains unclear.

Much of the existing literature captures the spatter and vapour plume over the powder surface using *in situ* high-speed optical [14, 22] or Schlieren imaging [29], which lack details on the changes of vapour depression or keyhole morphology during LPBF. Synchrotron x-ray sources can be used to capture both spatter and melt pool dynamics during LPBF at exceptional temporal resolution (up to 1 MHz) [30–34]. Combining synchrotron x-ray radiography and Schlieren imaging suggests that the vapour ejection angle is highly related to the morphology of the depression zone/keyhole [35]; however, the influence of keyhole morphology on spatter formation remains not well understood.

Here, we employed synchrotron radiography at a 40 kHz image acquisition rate to monitor and quantify the relationship between spatter ejection and vapour depression dynamics during LPBF of AA8A61.50 under varying industrially relevant process parameters. Our study emphasises that small spatter can induce unfavourable surface defects on LPBF parts, thereby highlighting the critical importance of understanding its behaviour to devise new printing strategies to avoid spatter and enhance LPBF quality.

2. Methods

2.1. Materials

The feedstock material was AA8A61.50 (Ahead® CP1, Constellium, France). The powder morphology and size distribution were characterised using scanning electron microscopy (SEM) under 20 kV (JEOL JSM-6610 LV, Tokyo), see details in supplementary figure S1.

2.2. *In situ* synchrotron x-ray imaging

The LPBF processing parameters (table 1) were selected to cover a range of linear energy densities (E_l) ranging from $210 \text{ J}\cdot\text{m}^{-1}$ to $840 \text{ J}\cdot\text{m}^{-1}$. E_l is calculated using:

$$E_l = \frac{PD}{v}, \quad (1)$$

Table 1. Processing parameters for LPBF of AA8A61.50 alloy.

Sample	Laser power, P (W)	Scan speed, v (mm·s ⁻¹)	Exposure time, t_e (μ s)	Delay time, t_d (μ s)	Linear energy density, E_l (J·m ⁻¹)
S1	350	800	40	10	350
S2	400	800	40	10	400
S3	450	800	40	10	450
S4	500	800	40	10	500
S5	420	500	20	0	840
S6	420	1000	20	0	420
S7	420	1500	20	0	280
S8	420	2000	20	0	210

where P is laser power, v is the scan speed and D is the duty cycle. When the laser operates in continuous wave (CW) mode, its duty cycle (D) is 100%. For pulse width modulation mode, we multiply a duty cycle of 80% to normalise the laser power. The duty cycle is defined by the ratio of laser exposure time, t_e at each of the semi-discrete points forming a scan vector with a delay time, t_d between consecutive points:

$$D = \frac{t_e}{t_e + t_d}. \quad (2)$$

We used high E_l conditions to replicate keyhole mode melting for contour scans to reduce surface roughness. Despite sub-surface keyhole porosity, such conditions can potentially improve the fatigue performance of AA8A61.50 parts. In contrast, we used low E_l conditions to replicate conduction mode melting for maximising LPBF productivity. However, a low E_l can lead to the formation of lack of fusion defects and increase scatter in mechanical properties. Laser welding on AA8A61.50 was also performed under the same processing conditions for comparison. The laser spot size is 80 μ m.

The abovementioned experiments were performed using bespoke AM machine, called the Quad-laser *in situ* and *operando* process replicator (Quad-ISOPR). The Quad-ISOPR comprises four lasers and the scan head of a RenAM 500Q (Renishaw plc., UK) system combined with a custom-built environmental chamber. A substrate with a 1 mm through-thickness and 15 mm height is mounted in the chamber onto which a thin layer of the powder is automatically deposited, see figure 1(a). The substrates were produced by LPBF using the same AA8A61.50 powder feedstock to mimic processing of a thin powder layer on top of a 15 mm tall AM part. Each substrate was mounted in a configuration depicted in [36]. Argon shielding gas was used during LPBF and laser welding.

The *in situ* experiments were carried out at the European Synchrotron Radiation Facility's (ESRF) high-speed imaging beamline ID19 [37]. This beamline employs two U32 undulators to produce a polychromatic hard x-ray beam with a mean energy of ~ 30 keV. Once the incident beam passes through the sample and glassy carbon windows on either side of the enclosure, the attenuated x-ray is converted by a LuAG: Ce scintillator and emits visible light. The visible light image is magnified by a $5\times$ objective and then captured by a high-speed camera (Photron FASTCAM SA-Z 2100K, Photron Ltd, Japan) at a framerate of 40 kHz. The

sample thickness was chosen to achieve $\sim 40\%$ x-ray attenuation through the substrate and glassy carbon stack according to the Beer-Lambert law. The field of view (FoV) was 1024 px (width) \times 512 px (height) with an isotropic pixel size of 4.3 μ m, giving a FoV of 4.4 mm \times 2.2 mm. Each scan track was 4 mm in length and was centred within the FoV of the x-ray image to capture the process dynamics during the onset, steady state, and end of laser scanning. The laser trigger, x-ray shutter opening, and image acquisition were synchronised using a PandABox (Quantum Detectors, Oxford, UK).

2.3. Surface roughness measurement

The surface profiles of all the build samples were imaged by a high-resolution optical microscopy (Keyence VHX-7000, Keyence, Japan). The surface roughness (R_q) was calculated through the measured height profiles [38] (see supplementary figure S2) via: $R_q = \sqrt{\frac{\sum_1^n (h_x - h_m)^2}{n}}$, where h_x is the measure heights along the building track, h_m is the mean height and n is the measured position number.

2.4. Image processing and quantification

The acquired radiographs were processed with ImageJ [39] and MATLAB[©] using a processing pipeline illustrated in figures 1(b)–(d). The radiographs were first corrected using $FFC = I_0 / \text{Flat}_{\text{ave}}$ [40], where FFC is the flat-field corrected image, I_0 is the raw radiograph, and Flat_{ave} is the average of 100 flat-field images. The dark signal is already subtracted by the camera software. A custom background subtraction (BS) was applied to remove stationary objects. The solid spatter and liquid droplet particles were segmented by applying a Gaussian filter and manual threshold value. The particle movement was tracked and quantified using the TrackMate plugin [41] in ImageJ by applying a mask detector and advanced Kalman Tracker (see examples in supplementary videos V1 and V2). The maximum number of frames over which a particle identified per track was set at 3. To capture the steady state keyhole or depression zone morphology, the BS images were re-framed to focus on the melt pool region in an Eulerian frame of reference using a bespoke Python script.

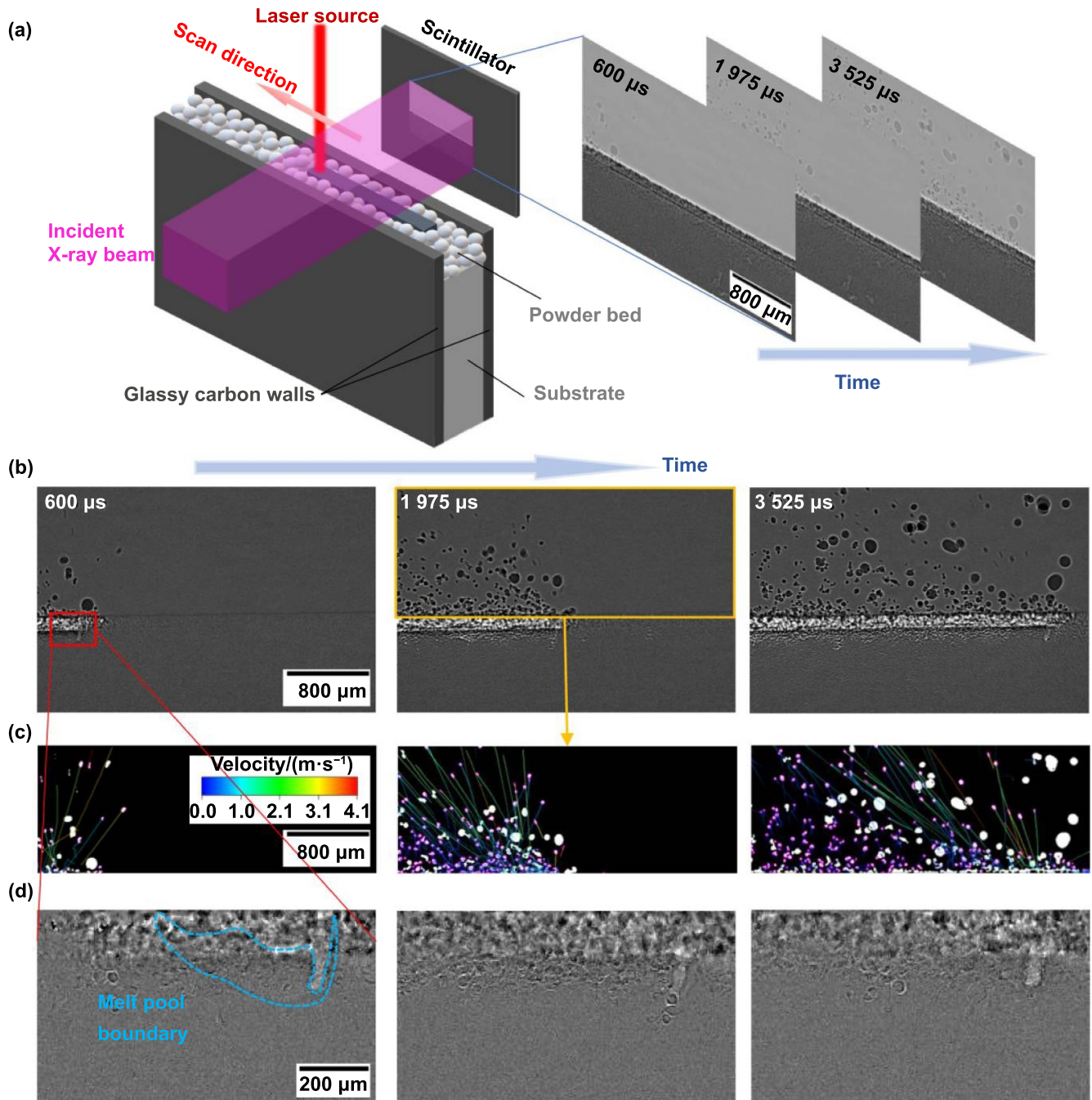


Figure 1. Evolution of a single melt track during LPBF of AA8A61.50 (Sample S2, $P = 400$ W, $v = 800$ mm·s⁻¹). (a) Schematic of *in situ* x-ray imaging set up during LPBF. (b) Sequential images of melt pool and spatter dynamics with flat-field correction and background subtraction. (c) Particle (solid spatter) tracking using TrackMate plugin in ImageJ, after segmentation by applying a Gaussian filter and manual threshold. The colour of the track indicates the spatter velocity. (d) Re-framed images focusing on the melt pool region.

3. Results and discussion

3.1. Identification of solid spatter, powder agglomeration and liquid spatter

We have classified five types of ejecta during LPBF and laser welding of AA8A61.50 using *in situ* x-ray imaging according to their formation mechanisms: ejected solid spatter, entrained solid spatter, powder agglomeration, jet spatter and large liquid

droplet, see x-ray radiographs in figures 2(a) and (b) and the corresponding schematic diagram in figure 2(c).

Two types of solid spatter are observed during LPBF: (1) the un-melted powder surrounding the melt pool that is ejected directly by the vapour plume under high vapour pressure—terms ejected solid spatter; (2) entrained solid spatter occurs when powder particles are entrained by a vortex flow of argon gas induced by the vapour plume and the wakefield of the scanning laser beam. The solid spatter accounts for >82% of the

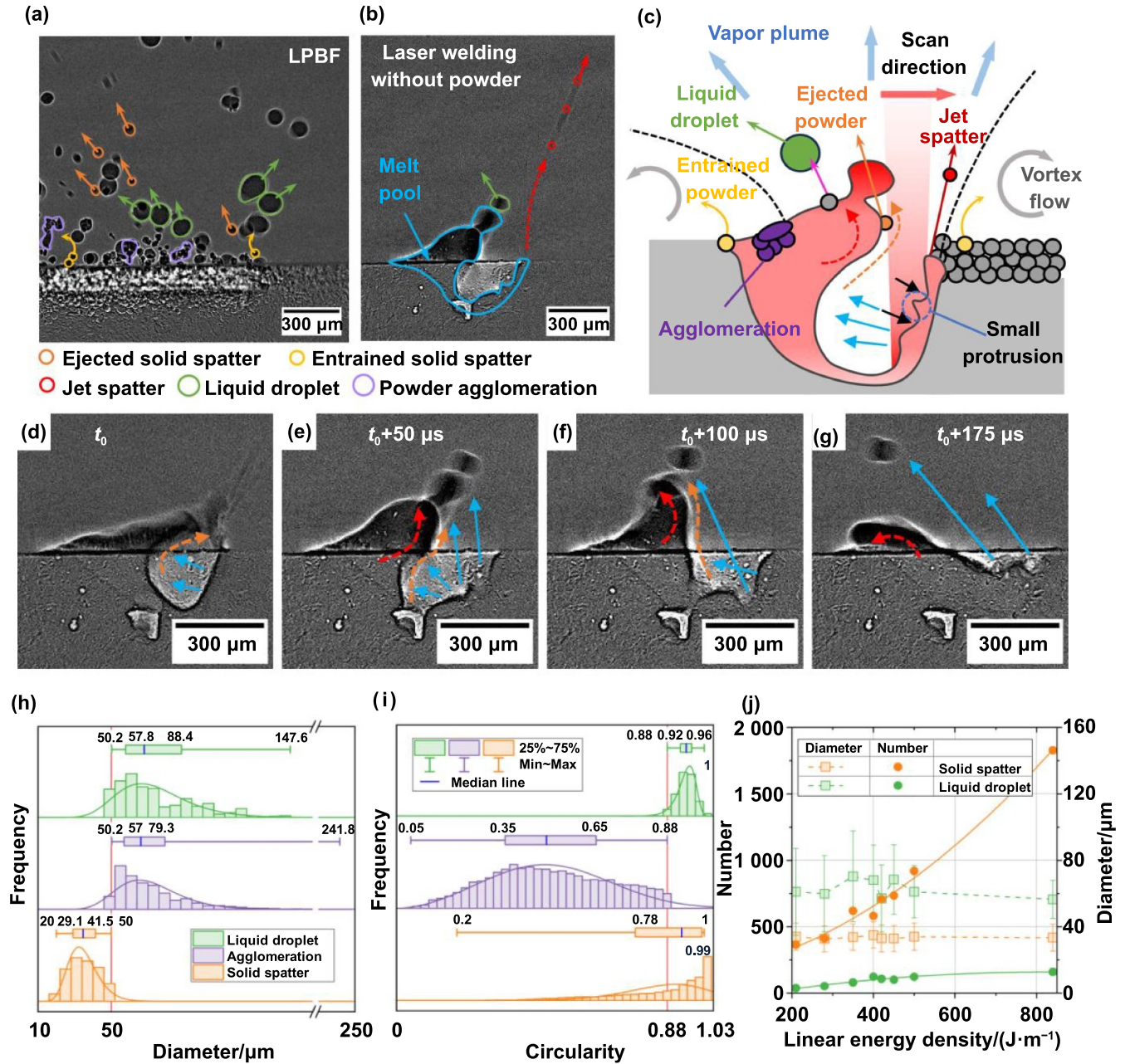


Figure 2. Identification of solid spatter, powder agglomeration, and liquid droplet during LPBF of AA8A61.50 (Sample S2, $P = 400 \text{ W}$, $v = 800 \text{ mm}\cdot\text{s}^{-1}$). X-ray image during LPBF with (a) powder and (b) laser welding without powder showing 5 spatter particle types distinguished with different colours. (c) Schematic of the corresponding melt pool and spatter behaviour; where orange, yellow, green and red solid arrows refer to the moving trend of ejected powder, entrained powder, liquid droplet and jet spatter motion. The pink solid arrow refers to the moving trend of powder into droplet. The black solid arrow indicates the recoil pressure, blue dot arrow indicates the vapour flow, generating the shear force (orange dot arrow) along rear keyhole wall, and red dot arrow indicates the Marangoni flow. (d)–(g) Imaging sequence indicating the formation mechanism of large liquid droplet. (h) Distribution of diameter and (i) circularity for solid spatter, liquid droplet and agglomeration. (j) Quantification of solid spatter/liquid droplet amount and diameter as a function of linear energy density and number (N)-Linear energy density (E_l) curve fits.

total ejecta. Their size and circularity (as shown in figures 2(h) and (i)) match the powder feedstock size distribution (see supplementary figure S1).

The powder particles close to the melt pool boundary can be partially melted or sintered by the scanning laser beam, forming powder agglomerations. This agglomerate spatter exhibits a larger particle size and a lower circularity (<0.88) compared

to the solid spatter, see figures 2(h) and (i), respectively. Most of these agglomerates were carried away from the laser-matter interaction zone and then entrained by the argon gas flow.

The formation of liquid spatter can be caused by the complex interplay among the melt flow, the high vapour pressure/recoil pressure generated by metal vaporisation, and the surface tension of the liquid metal. The liquid spatter generated

from melt pool is more visible during laser welding compared to LPBF under same conditions, see figures 2(b) and (d)–(g). The localised recoil pressure on the front keyhole wall first generates a small melt protrusion. When the protrusion reaches the rim of the front keyhole wall by the melt flow, it pinches off causing jet spatter. Our observed jet spatter mechanism is different to the bulk-explosion event from [24]. Such jet spatter observed during laser welding without powder is smaller or equivalent to the solid spatter, however, it only accounts for $\sim 2\%$ of the total number of spatter instances under the conditions studied.

Apart from the above small jet spatter, we observed a new mechanism by which large liquid droplets form at the rear rim of the keyhole. Under keyhole melting conditions, the Marangoni flow [42] pushes the liquid metal near the keyhole bottom towards the top melt pool surface. The intense vapour flow (blue solid arrow) induces vapour pressure towards the rear keyhole wall (figure 2(d)). Previous work estimates that the vapour jet velocities can reach from $20 \text{ m}\cdot\text{s}^{-1}$ [43] to $300 \text{ m}\cdot\text{s}^{-1}$ [29] whereas the melt flow can only reach up to $5 \text{ m}\cdot\text{s}^{-1}$ [43]. The differences in velocities and densities between metal vapour and liquid metal induce a perturbation at the gas/vapour-liquid interface, *a.k.a.* Kelvin–Helmholtz instability [44, 45], which also imposes a shear force along the gas-liquid interface (orange dotted arrow). The combination of the Kelvin-Helmholtz instability and Marangoni convection (red dotted arrow) promotes the formation of a large liquid protrusion at the rear wall (figure 2(e)). If the liquid protrusion is sufficiently large, it may amalgamate into the melt pool again under surface tension [23]. As the vapour jet continues to interact with the protrusion, it superheats the liquid metal and decreases its surface tension, forming a neck region. Once the vapour pressure overcomes the surface tension of the neck region, a large liquid droplet is detached (figure 2(f)) and then ejected by the vapour plume (figure 2(g)).

The average diameter of liquid droplets ejected during laser welding ($(43 \pm 12) \mu\text{m}$) is smaller than those formed during LPBF ($(68 \pm 21) \mu\text{m}$). This confirms the powder-droplet/droplet-droplet coalescence events (see supplementary figure S3) are another formation mechanism of liquid droplet during LPBF, matching the observation reported in [25]. The size of the liquid droplets in LPBF is comparable to the powder agglomerations (figure 2(h)) yet can be distinguished by their higher circularity (figure 2(i)).

Figure 2(j) shows no correlation between spatter size distribution and linear energy density (E_l) as the equivalent diameters of solid spatter/liquid droplet are of similar magnitudes across the E_l range. However, it shows a strong positive correlation between the number of solid spatter (N_{solid}) or liquid droplet (N_{droplet}) and E_l . Therefore, we have deduced the following equations to predict the number of spatters during LPBF of AA8A61.50:

$$N_{\text{solid}} = (139 \pm 129) + (0.6 \pm 0.5) \cdot E_l + (0.016 \pm 0.0005) \cdot E_l^2 \quad (3)$$

for solid spatter ($R^2 = 0.99$) and

$$N_{\text{droplet}} = (-67 \pm 33) + (0.6 \pm 0.1) \cdot E_l - (0.0003 \pm 0.0001) \cdot E_l^2 \quad (4)$$

for liquid droplets ($R^2 = 0.92$), where E_l ranges from $210 \text{ J}\cdot\text{m}^{-1}$ to $840 \text{ J}\cdot\text{m}^{-1}$. Both equations can be used for future model validation and to devise new printing strategies for minimising spatter.

3.2. Quantification of solid spatter and liquid droplet motion

To understand the spatter dynamics across different scan velocities and laser powers, we have tracked and quantified the trajectory angle, fraction, and velocity of solid spatter particles and liquid droplets during LPBF, see figure 3. The respective velocity and angle distributions are detailed in supplementary figures S4 and S5. The spatter is further divided into backward and forward spatter types based on their trajectory angles relative to the laser beam position (0°), see inset in figure 3(a). The backward spatter has a trajectory angle spanning from -90° to 0° , with the rest (0° – 90°) considered as forward spatter. Possible quantification errors could be due to the overlapping particles and particles that move in and out of the page of the radiographs.

We also compare the kinetic energy of spatter, E_k , with the input laser energy, E_i , to estimate the percentage of energy consumed by the spatter generation process, $P_E = \frac{E_k}{E_i} = \frac{\sum mv_m^2}{2E_i L} \times 100\%$, where L is the track length, and m and v_m are the mass and velocity of individual spatter, respectively. The mass of spatter is given as $m = \frac{4}{3}\pi r^3 \rho$, where r is the equivalent radius of spatter, ρ is the density of spatter which is taken as 2710 and $2385 \text{ kg}\cdot\text{m}^{-3}$ for solid and liquid aluminium, respectively [46].

Figure 3(a) shows a negligible effect of increasing the laser power from 350 W to 500 W on the average trajectory angle at a constant scan speed of $800 \text{ mm}\cdot\text{s}^{-1}$, which remains from -10° to -25° across all laser powers. Under these conditions, most ejecta are backward spatter (70% – 80%).

Figure 3(b) shows that most ejecta remain as backward spatter (ejected angle $< -18^\circ$) at a scan speed between $1000 \text{ mm}\cdot\text{s}^{-1}$ and $2000 \text{ mm}\cdot\text{s}^{-1}$ and a constant laser power of 420 W . Given that the vapour depression zone is four times wider than the typical keyhole aperture observed in our study, the high-velocity vapour plume is more likely to interact with spatter, inducing more backward liquid droplets ($>90\%$). The average ejection angle of solid spatter/liquid droplets reduces to $\sim 0^\circ$ when the scan speed decreases to $500 \text{ mm}\cdot\text{s}^{-1}$, which is closely linked to the keyhole morphology, see explanation later.

Figure 3(c) demonstrates a strong positive correlation between laser power and spatter velocities/kinetic energy, owing to that higher laser power (or high E_l) would induce more metal vaporisation and spatter during LPBF. The spatter velocity magnitude of AA8A61.50 is comparable to other Al systems, such as Al10SiMg [20, 33], however, it is $2 \sim 3$ times higher than that of Ni alloys [23].

Figure 3(d) also shows an increased trend of kinetic energy with decreased scan speed (or increased E_l). However, an

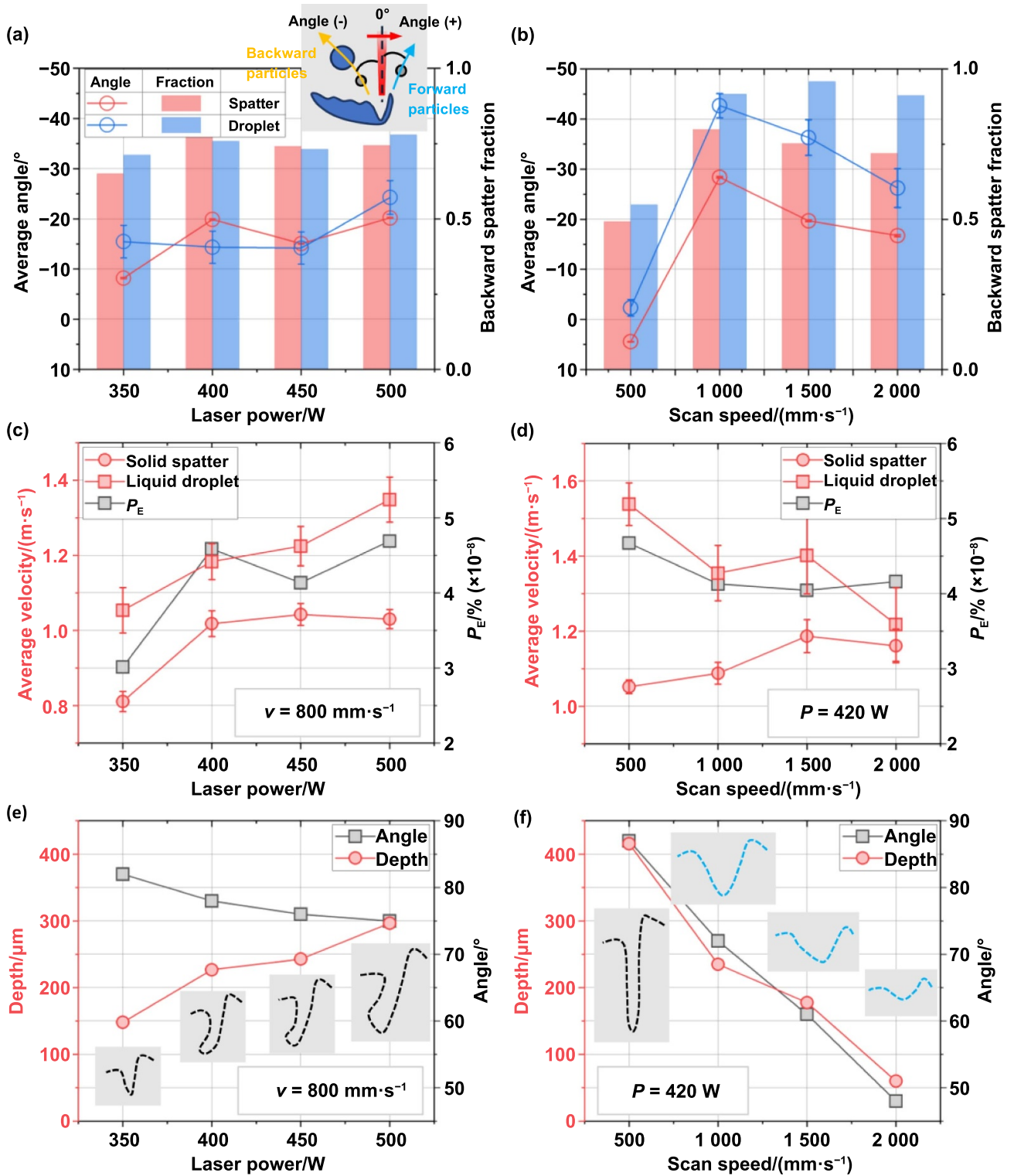


Figure 3. Quantification of solid spatter/liquid droplet dynamics during LPBF: (a) average trajectory angle (line graph) and backward spatter fraction (bar chart) as a function of laser power (quantified from sample S1–S4) and (b) as a function of scan speed (quantified from sample S5–S8). (c) Average spatter velocity and P_E as a function of laser power and (d) as a function of scan speed. (e) Keyhole/depression zone depth and front wall angle (θ) as a function of laser power and (f) as a function of scan speed. The black and blue dotted lines depict keyhole and depression zone, respectively.

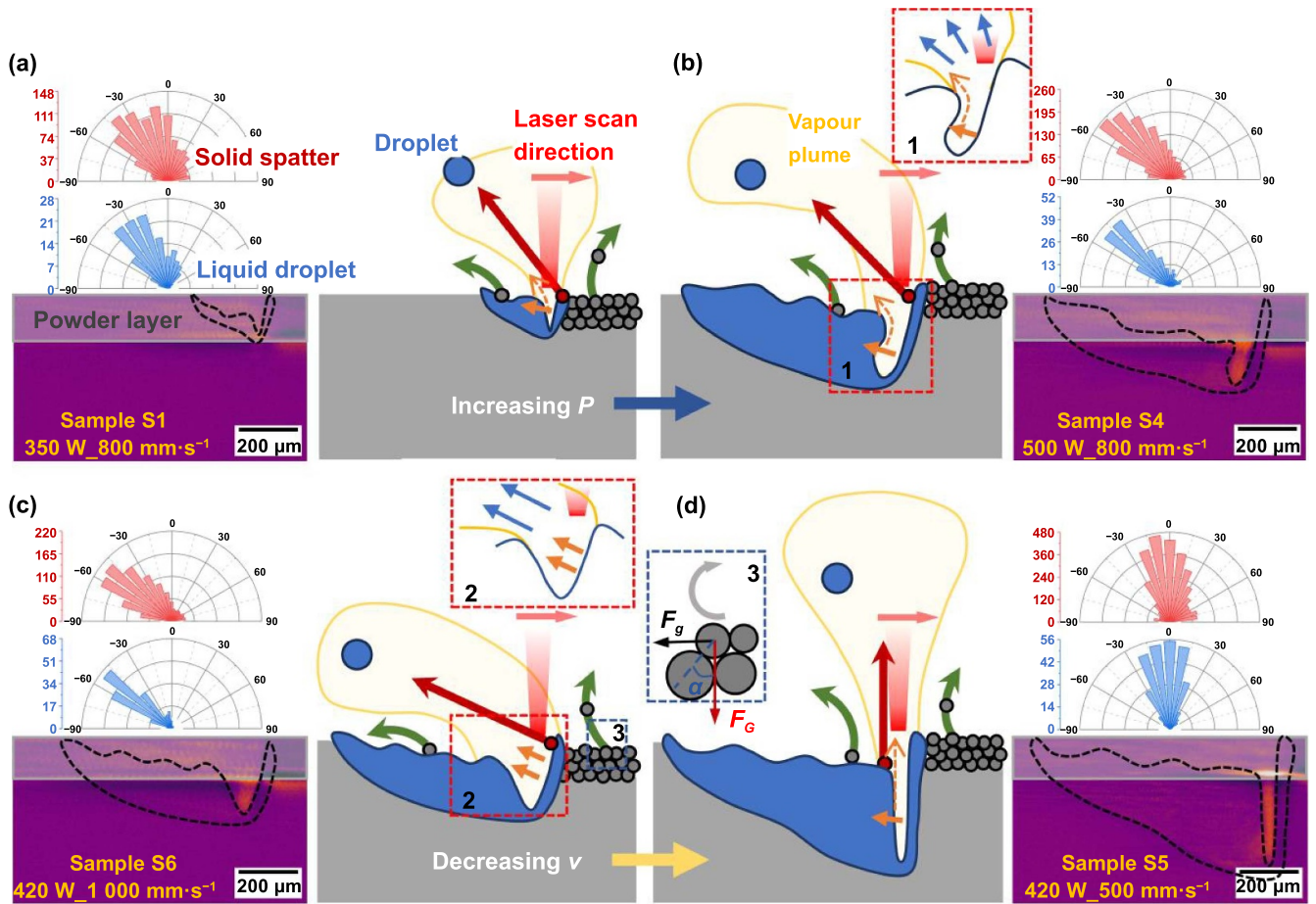


Figure 4. Schematic depicting the correlation between solid spatter/liquid droplet motion with keyhole/depression zone morphology, where (a) and (b) present the effect of increased laser power, and (c) and (d) present the effect of decreased scan speed. The red and green solid arrows indicate the motions of ejected solid and entrained solid spatter, respectively. The orange solid arrow indicates the vapour flow caused by metal vaporisation in the front depression zone/keyhole wall, and the orange dotted arrow indicates the reflection of vapour plume under keyhole mode. Insets 1 and 2 illustrate different vapour plume direction (blue solid arrow) under keyhole and conduction modes. Inset 3 illustrates particle entrainment induced by the Argon vortex flow (gray solid arrow) under drag force, F_g .

inverse particle velocity-scan speed relationship between solid spatter and liquid droplets can be observed, which is due to the increase of powder entrainment, see explanation in section 3.3.2.

Figure 3(e) shows an increase in keyhole depth with increasing laser power, but there are negligible changes in keyhole morphology and spatter angle, see figure 3(a); this remains true when the front keyhole wall angle (θ) is $< 82^\circ$. A reduction in scan speed from $2000 \text{ mm}\cdot\text{s}^{-1}$ to $1000 \text{ mm}\cdot\text{s}^{-1}$ at 420 W laser power continues to increase the surface area of the depression zone, depth, and θ , see figure 3(f). As the scan speed further reduces $500 \text{ mm}\cdot\text{s}^{-1}$, the vapour depression zone transforms into a deep 'T'-shaped keyhole, promoting forward spatter. Based on our analysis in figures 2–3, the scan speed has a stronger influence on the spatter trajectory angle than laser power, therefore we would recommend that faster scan velocities or low E_l can reduce θ and spatter during LPBF of AA8A61.50.

3.3. Correlation between solid spatter/liquid droplet motion and keyhole morphology

3.3.1. Spatter trajectory angles.

Here, we have selected four processing conditions to explain how the front keyhole wall angle and the keyhole morphology change the spatter trajectory angle. Figures 4(a) and S4 reveal the formation of a small, cone-shaped, near-vertical keyhole under a laser power of 350 W and a medium scan speed of $800 \text{ mm}\cdot\text{s}^{-1}$. Figure 4(b) shows an inclined 'J'-shaped keyhole as the laser power increases to 500 W . The dominant vapour flow (orange solid arrow) is generated at the hottest region (or the front wall) of the vapour depression zone/keyhole [22]. Once the initial vapour plume reaches the rear keyhole wall, it deflects upward (orange dotted arrow), see illustration in **inset 1**. The resultant spatter has a steeper ejection angle (red solid arrow), distinct from the direction of the initial metal vaporisation (orange solid arrow).

Figure 4(c) shows that a high scan speed ($>1000 \text{ mm}\cdot\text{s}^{-1}$) promotes the formation of a shallow quasi-semi-circular-shaped depression zone, with a front wall angle of $<72^\circ$ (figure 3(f)). The vapour pressure generated from the shallow front wall of the quasi-semi-circular depression zone promotes spatter mostly in a negative spatter ejection angle in the same direction as the vapour plume (see **inset 2**). Figure 4(d) illustrates a more deeply penetrating 'I'-shaped keyhole is formed at the slow scan speed of $500 \text{ mm}\cdot\text{s}^{-1}$. The vapour plume impinges on the rear keyhole wall and further redirects along it, driving the spatter upwards.

In summary, the vapour pressure is the main driving force attributed to the spatter ejection direction during LPBF which is correlated to different keyhole geometries as quantified in figures 3 and 4. Increasing the laser power from 350 W to 500 W with a scan speed of $800 \text{ mm}\cdot\text{s}^{-1}$ leads to a twofold increase in keyhole depth, but this has minimal change in keyhole morphology and spatter trajectory. However, decreasing the scan speed from $2000 \text{ mm}\cdot\text{s}^{-1}$ to $500 \text{ mm}\cdot\text{s}^{-1}$ with 420 W laser power changes the depression zone morphology from vapour depression to keyhole. The increase in both depression depth and front wall angle causes a shift from shallow-angle backward spatter to predominantly vertical spatter. Similar observations (correlation of E_l , depression zone morphology and vapour trajectory) have been reported in [35], however, it mainly focused on the vapour plume behaviour and did not correlate spatter dynamics, e.g. velocities and trajectory angles, with other features such as front wall angle, keyhole geometry, or processing parameters.

3.3.2. Solid spatter/liquid droplet velocity. Figures 3(c) and (d) show that the overall kinetic energy of solid spatter and liquid droplets increases with increasing E_l through either increasing P or decreasing v . An increase in E_l will lead to a high melt pool temperature and more metal vaporisation [47], resulting in higher recoil and vapour pressure, and increasing spatter (figure 2(e)). To confirm this hypothesis, we have quantified the recoil pressure, P_r , induced by the metal vaporisation process, and calculated the saturated vapour pressure, P_s [48] over a melt pool surface. This is given by [47]:

$$P_r = 0.56P_s. \quad (5)$$

$$P_s = P_0 \exp\left(\frac{\Delta H_V}{R} \frac{T - T_b}{T^* T_b}\right), \quad (6)$$

where P_s is the vapour pressure, P_0 is the atmospheric pressure (1 atm), ΔH_V is the latent heat of vaporisation, which is $291 \text{ KJ}\cdot\text{mol}^{-1}$ for aluminium [47], T_b is the boiling temperature of Al, which is 2773 K [47], and R is the gas constant, which is $8.3 \text{ J}\cdot\text{mol}^{-1}\cdot\text{K}^{-1}$. The peak temperature, T , at the melt pool surface processed by a stationary Gaussian beam can be estimated by [48]:

$$T = \frac{\sqrt{2}AI\sigma}{\kappa\sqrt{\pi}} \tan^{-1} \sqrt{\frac{2\lambda}{v\sigma}}, \quad (7)$$

where A is the absorptivity (0.58 [49]), σ is laser spot size of $80 \mu\text{m}$, κ is the thermal diffusivity, taken as $89.3 \text{ W}\cdot\text{mK}^{-1}$ [50] for liquid Al, λ is thermal conductivity of molten Al, which is $3.3 \times 10^{-5} \text{ m}^2\cdot\text{s}^{-1}$ [50], and I is the laser intensity calculated by: $I = P/2\pi\sigma^2$. Combining equations (5)–(7), the calculated recoil pressure increases from 3.1 atm to 83.2 atm as P increases from 350 W to 500 W at $800 \text{ mm}\cdot\text{s}^{-1}$ and increases from 0.6 atm to 62.1 atm with decreased v from 2000 to $500 \text{ mm}\cdot\text{s}^{-1}$ at 420 W. The velocity of recoil/vapour pressure driven spatter increases with both increased P and decreased v (or increased E_l). However, a drop in solid spatter velocity with decreasing v is evident for the solid particles, as shown in figure 3(d). The increased proportion of entrained solid spatter with a lower spatter velocity compared to the ejected solid spatter, is hypothesised to be the underlying reason for this.

The **inset 3** in figure 4 illustrates a drag force, F_g , is exerted on the entrained solid spatter by an outward argon vortex flow and estimated by [51]:

$$F_g = 0.5\rho_g C_x S U^2, \quad (8)$$

where ρ_g is the Argon density, C_x is the drag coefficient, S is the particle's projected area and U is the Argon flow velocity. The criterion of particle entrainment is defined as:

$$F_g \geq F_G \tan \alpha, \quad (9)$$

where F_G is the weight of the entrained particle and α is the contact angle between two particles. A pressure drop occurs inside the vapour plume as a result of the velocity increase when vapour flows out from the constriction at the keyhole/depression zone opening according to the Bernoulli Effect [52]. This pressure difference accelerates the surrounding argon towards the vapour depression zone, which in turn causes the formation of an argon vortex flow. Powder entrainment occurs when the F_g exceeds the critical value according to equation (7). Decreasing the scan speed reduces the keyhole/depression zone opening volume, and hence creates a stronger argon vortex flow under an enhanced Bernoulli Effect. Therefore, we expect a high proportion of entrained solid spatter as the F_g increases, according to equation (6). The calculated outward argon flow velocity above the powder bed is up to $\sim 7 \text{ m}\cdot\text{s}^{-1}$ [51] and two orders of magnitude slower than the vapour plume velocity. As a result, the velocity of the entrained solid spatter is expected to be slower than that of the ejected solid spatter, similar to observations reported in [33]. The increased proportion of entrained solid spatter with decreased scan speed explains the corresponding decrease in average solid spatter velocity.

In summary, both the spatter velocity and the kinetic energy generally increase with higher E_l (increased P or decreased v) due to the higher vapour pressure and recoil pressure. Additionally, the depression zone morphology changes from a shallow depression zone to deep keyhole as a result of decreased v , reducing the overall average solid spatter velocity by inducing increased powder entrainment.

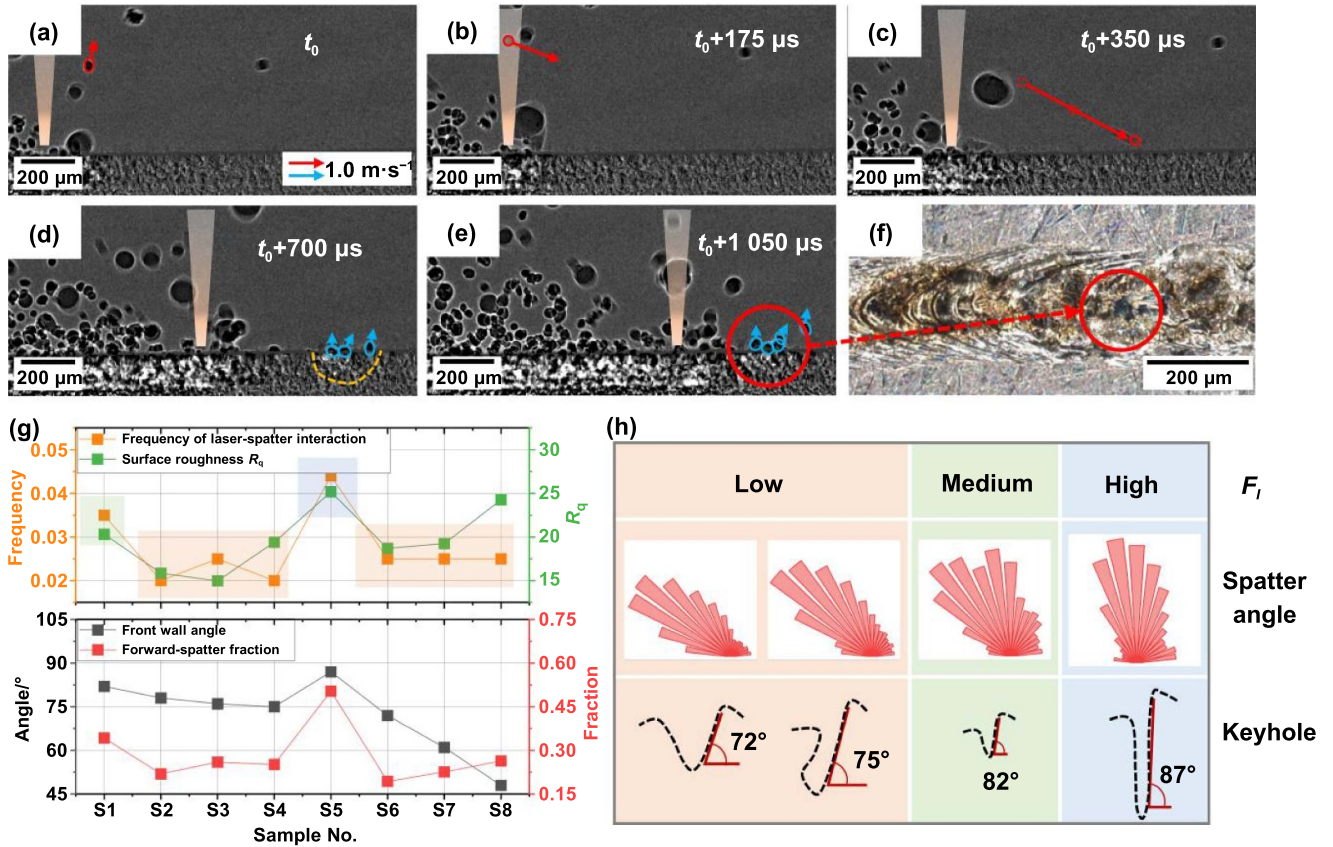


Figure 5. Laser-spatter interaction and its impact on the track surface. (a)–(e) Time-resolved x-ray images showing ejected spatter impacting the powder bed after interaction with the moving laser beam for sample S3 ($P = 450 \text{ W}$, $v = 800 \text{ mm}\cdot\text{s}^{-1}$). Red arrows indicate the velocity vectors of the spatter particle, and the blue arrows indicate those of the impacted powder particles. (f) Optical image of the surface defect induced by the laser-spatter interaction. (g) The correlated keyhole/depression zone front wall angle, forward-spatter fraction, frequency of laser-spatter interaction (F_I), and surface roughness as a function of processing parameters. (h) Schematic depicting the relationship between laser-spatter interaction frequency, ejection angle, and the morphology of the keyhole/depression zone.

3.4. Interaction between laser beam and solid spatter

Previous studies [15, 25, 26] show that large liquid droplets can be trapped between layers inducing impurities and lack-of-fusion porosity, detrimental to the properties of LPBF products. Figure 5 illustrates a new type of defect, namely a spatter-induced cavity, that is induced by the solid powder spatter interacting with the laser beam during flight. A forward spatter particle ($\sim 36 \mu\text{m}$) is first ejected into the laser scanning path (figure 5(a)) and then changes its spattering direction towards the powder bed after the laser-spatter interaction under a laser radiation force, F_{rad} (figure 5(b)), which can be estimated using the following equation [53]:

$$F_{\text{rad}} = \frac{2qP}{c}, \quad (10)$$

where q is the laser reflection coefficient, which is taken as 0.8 for Al particles with oxidation [54], P is the laser power and c is the speed of light.

At a laser power of 450 W, the calculated F_{rad} is $2.4 \times 10^{-6} \text{ N}$. The spatter changes its trajectory from upward

to downward and accelerates from $0.57 \text{ m}\cdot\text{s}^{-1}$ along its initial path to $3.39 \text{ m}\cdot\text{s}^{-1}$ over $350 \mu\text{s}$, prior to colliding with the powder bed. The critical force required by a spatter to maintain its original trajectory can be estimated by $F_c = ma$, which is $1.0 \times 10^{-6} \text{ N} < F_{\text{rad}}$. Upon the collision (figure 5(c)), this induces further powder spatter at the powder bed (figures 5(d) and (e)), forming a localised denudation zone ahead of the laser beam and a surface cavity in the final deposited layer after laser melting (figure 5(f)). Such spatter-induced surface cavity could act as a crack initiation site for fatigue failure [55].

We also observed multiple laser-spatter interactions during LPBF. In the first instance, a small spatter agglomerate interacts with the laser beam (supplementary figure S6) and then transforms into a liquid droplet ($47 \mu\text{m}$). Upon further laser-droplet interaction, the droplet alters its trajectory and accelerates towards the powder layer thereby causing a spatter-induced surface cavity. This phenomenon occurs when $F_c < F_{\text{rad}}$ satisfies, in which F_c is $1.4 \times 10^{-6} \text{ N}$ and F_{rad} is $2.2 \times 10^{-6} \text{ N}$. In the second instance, a larger liquid droplet ($\sim 130 \mu\text{m}$ in size) is generated from a similar laser-powder agglomerate interaction (supplementary figure S7), the F_{rad} ($2.2 \times 10^{-6} \text{ N}$) is insufficient to change the trajectory of the large droplet as it has a much larger F_c

(9.5×10^{-6} N), i.e. $F_c > F_{\text{rad}}$ in this case. To minimise spatter-induced surface cavities, the end-users should minimise F_{rad} , avoid small powder size fractions and use uniform powder size distribution.

Figure 5(g) demonstrates the correlated front wall angles of the keyhole/depression zone, forward-spatter fraction, frequency of laser-spatter interaction (F_I), and surface roughness as a function of processing parameters, divided into three distinct levels of interaction frequency: low (orange), medium (green), and high (blue). A shallow keyhole/depression zone front wall angle (such as samples S2–S4 and S6–S8 in figure 5(g)) creates minimal forward spatter. Reducing forward spatter (which may interact with the laser) should lead to decreased laser-spatter interaction events, hence reducing surface cavities and improving the surface quality (i.e. low surface roughness). Figure 5(h) further interprets the influence of keyhole/depression zone morphology on the laser-spatter interaction frequency. Quasi-semi-circular depression zones or ‘J’-shaped keyholes with relatively low front wall angles ($\sim 70^\circ$) tend to result in a lower fraction ($< 25\%$) of forward spatter and hence low frequency of spatter-laser interaction events. As the keyhole front wall angle becomes steeper (at an angle of 82°), a corresponding increase in the frequency of laser-spatter interaction was observed with the associated higher possibility of surface cavity formation and decreased surface quality (i.e. high surface roughness). Our results confirm that a high keyhole front wall angle (87°) is the key factor leading to a high frequency of laser-spatter interaction and spatter-induced cavities during LPBF.

4. Conclusions

The interrelated dynamics of spatter and keyhole formation during LPBF of an aluminium alloy, AA8A61.50 (Aheadd® CP1) were characterised using *in situ* synchrotron x-ray imaging.

Five distinct spatter particle types are classified based on their differing size and circularity characteristics: ejected solid spatter, entrained solid spatter, jet spatter, liquid droplets, and powder agglomerations. Additionally, we discovered two new spatter mechanisms during LPBF:

- (i) **Rear rim droplet spatter**—occurs when the metal vapour jet overcomes the surface tension of the protrusion induced by the combination of Kelvin-Helmholtz instability and the Marangoni convection at the rear rim of the keyhole. The observed droplet formation mechanism in high-speed welding is indicative of that in LPBF under the same conditions, due to the observed similarity in keyhole shape and size when the powder layer is less than $60 \mu\text{m}$ [35, 56]. Therefore, the effect of powder on the vapour dynamics is expected to be similarly minimal.
- (ii) **Spatter-induced surface cavity**—occurs when the laser radiation force exceeds the critical force acting on the particle during laser-spatter interaction. A high keyhole

front wall angle (87°) leads to a high frequency of laser-spatter interaction and spatter-induced cavities during LPBF.

We quantified the dynamics of solid spatter and liquid droplets during LPBF, e.g. size distribution, trajectory angle, spatter velocity and kinetic energy, and formulated two equations to predict spatter. Additionally, we correlated these measurements with the keyhole/depression zone morphologies as a function of linear energy density.

Our results reveal that the scan speed has a stronger influence on the spatter trajectory angle than laser power. We would recommend that faster scan speeds ($> 1\,000 \text{ mm}\cdot\text{s}^{-1}$ with laser power of 420 W), or lower E_l (in an appropriate range that avoids the formation of lack-of-fusion defect), should be used to reduce the front wall angle and increase the vapour depression zone opening area during LPBF of AA8A61.50.

Acknowledgments

The authors are grateful for the support from the UKRI—EPSRC, Grants Numbered EP/W006774/1, EP/P006566/1, EP/W003333/1, and EP/V061798/1. PDL is funded by the support from a Royal Academy of Engineering Chair in Emerging Technologies (CiET1819/10); CLAL is funded in part by EP/W037483/1 and IPG Photonics/ Royal Academy of Engineering Senior Research Fellowship in SEARCH (ref: RCSRF2324-18-71). This research used resources of the European Synchrotron Radiation Facility (ESRF) in Beamline ID19 (ME-1573). Many thanks to team members from the Materials, Structure and Manufacturing group at Harwell (MSM@H) for their assistance in preparation for and during the beamtime.

Author contributions

C L A L and P D L conceived the Project. C L A L, R L G and S H led the experimental design and the experiments, with all authors contributing. DG led the data analysis, with all authors contributing. X F and D G conducted the S E M. R L G performed the surface roughness analysis. D G, C L A L, and P D L led the results interpretation and manuscript writing, with all authors contributing.

ORCID iDs

Da Guo  <https://orcid.org/0000-0003-2055-6762>
 Alexander Rack  <https://orcid.org/0000-0001-9486-3621>
 Peter D Lee  <https://orcid.org/0000-0002-3898-8881>
 Chu Lun Alex Leung  <https://orcid.org/0000-0002-4153-7512>

References

- [1] Khairallah S A, Anderson A T, Rubenchik A and King W E 2016 Laser powder-bed fusion additive manufacturing:

- physics of complex melt flow and formation mechanisms of pores, spatter, and denudation zones *Acta Mater.* **108** 36–45
- [2] MacDonald E and Wicker R 2016 Multiprocess 3D printing for increasing component functionality *Science* **353** aaf2093
 - [3] Wang Y M *et al* 2018 Additively manufactured hierarchical stainless steels with high strength and ductility *Nat. Mater.* **17** 63–71
 - [4] Sun X Y, Chen M N, Liu T T, Zhang K, Wei H L, Zhu Z G and Liao W H 2024 Characterization, preparation, and reuse of metallic powders for laser powder bed fusion: a review *Int. J. Extrem. Manuf.* **6** 012003
 - [5] Gao W, Zhang Y B, Ramanujan D, Ramani K, Chen Y, Williams C B, Wang C C L, Shin Y C, Zhang S and Zavattieri P D 2015 The status, challenges, and future of additive manufacturing in engineering *Comput.-Aided Des.* **69** 65–89
 - [6] Liu Z Z, Zhou Q H, Liang X K, Wang X B, Li G C, Vanmeensel K and Xie J X 2024 Alloy design for laser powder bed fusion additive manufacturing: a critical review *Int. J. Extrem. Manuf.* **6** 022002
 - [7] Brock L, Ogunsanya I, Asgari H, Patel S and Vlasea M 2021 Relative performance of additively manufactured and cast aluminum alloys *J. Mater. Eng. Perform.* **30** 760–82
 - [8] Ballardini R M, Flores Ituarte I and Pei E J 2018 Printing spare parts through additive manufacturing: legal and digital business challenges *J. Manuf. Technol. Manage.* **29** 958–82
 - [9] Kusoglu I M, Gökce B and Barcikowski S 2020 Research trends in laser powder bed fusion of Al alloys within the last decade *Addit. Manuf.* **36** 101489
 - [10] Zhao L, Song L B, Santos Macías J G, Zhu Y X, Huang M S, Simar A and Li Z H 2022 Review on the correlation between microstructure and mechanical performance for laser powder bed fusion AlSi10Mg *Addit. Manuf.* **56** 102914
 - [11] Martin J H, Yahata B D, Hundley J M, Mayer J A, Schaedler T A and Pollock T M 2017 3D printing of high-strength aluminium alloys *Nature* **549** 365–9
 - [12] Association A 2006 *Designations and Chemical Composition Limits for Aluminum Alloys in the Form of Castings and Ingot* (The Aluminum Association)
 - [13] Pauzon C, Buttard M, Després A, Charlot F, Fivel M, Chehab B, Blandin J J and Martin G 2023 Direct ageing of LPBF Al-1Fe-1Zr for high conductivity and mechanical performance *Acta Mater.* **258** 119199
 - [14] Zheng H, Li H X, Lang L H, Gong S L and Ge Y L 2018 Effects of scan speed on vapor plume behavior and spatter generation in laser powder bed fusion additive manufacturing *J. Manuf. Process.* **36** 60–67
 - [15] Wang D, Wu S B, Fu F, Mai S, Yang Y Q, Liu Y and Song C H 2017 Mechanisms and characteristics of spatter generation in SLM processing and its effect on the properties *Mater. Des.* **117** 121–30
 - [16] Ikeshoji T T, Yonehara M, Kato C, Yanaga Y, Takeshita K and Kyogoku H 2022 Spattering mechanism of laser powder bed fusion additive manufacturing on heterogeneous surfaces *Sci. Rep.* **12** 20384
 - [17] Kelly D, Fischer R D, Moaven M, Morris S, Prorok B C and Thurow B 2023 Simultaneous 3D tracking and temperature measurements of L-PBF spatter particles using a single camera *Addit. Manuf. Lett.* **6** 100134
 - [18] Esmailizadeh R, Ali U, Keshavarzkermani A, Mahmoodkhani Y, Marzbanrad E and Toyserkani E 2019 On the effect of spatter particles distribution on the quality of Hastelloy X parts made by laser powder-bed fusion additive manufacturing *J. Manuf. Process.* **37** 11–20
 - [19] Eschner E, Staudt T and Schmidt M 2019 3D particle tracking velocimetry for the determination of temporally resolved particle trajectories within laser powder bed fusion of metals *Int. J. Extrem. Manuf.* **1** 035002
 - [20] Young Z A, Guo Q L, Parab N D, Zhao C, Qu M L, Escano L I, Fezzaa K, Everhart W, Sun T and Chen L Y 2020 Types of spatter and their features and formation mechanisms in laser powder bed fusion additive manufacturing process *Addit. Manuf.* **36** 101438
 - [21] Chen H and Yan W T 2020 Spattering and denudation in laser powder bed fusion process: multiphase flow modelling *Acta Mater.* **196** 154–67
 - [22] Ly S, Rubenchik A M, Khairallah S A, Guss G and Matthews M J 2017 Metal vapor micro-jet controls material redistribution in laser powder bed fusion additive manufacturing *Sci. Rep.* **7** 4085
 - [23] Leung C L A, Marussi S, Towrie M, Atwood R C, Withers P J and Lee P D 2019 The effect of powder oxidation on defect formation in laser additive manufacturing *Acta Mater.* **166** 294–305
 - [24] Zhao C, Guo Q L, Li X X, Parab N, Fezzaa K, Tan W D, Chen L Y and Sun T 2019 Bulk-explosion-induced metal spattering during laser processing *Phys. Rev. X* **9** 021052
 - [25] Nassar A R, Gundermann M A, Reutzel E W, Guerrier P, Krane M H and Weldon M J 2019 Formation processes for large ejecta and interactions with melt pool formation in powder bed fusion additive manufacturing *Sci. Rep.* **9** 5038
 - [26] Taheri Andani M, Dehghani R, Karamooz-Ravari M R, Mirzaeifar R and Ni J 2017 Spatter formation in selective laser melting process using multi-laser technology *Mater. Des.* **131** 460–9
 - [27] Iantaffi C, Leung C L A, Chen Y H, Guan S L, Atwood R C, Lertthanasarn J, Pham M S, Meisnar M, Rohr T and Lee P D 2021 Oxidation induced mechanisms during directed energy deposition additive manufactured titanium alloy builds *Addit. Manuf. Lett.* **1** 100022
 - [28] Simonelli M, Tuck C, Aboulkhair N T, Maskery I, Ashcroft I, Wildman R D and Hague R 2015 A study on the laser spatter and the oxidation reactions during selective laser melting of 316L stainless steel, Al-Si10-Mg, and Ti-6Al-4V *Metall. Mater. Trans. A* **46** 3842–51
 - [29] Bidare P, Bitharas I, Ward R M, Attallah M M and Moore A J 2018 Fluid and particle dynamics in laser powder bed fusion *Acta Mater.* **142** 107–20
 - [30] Chen Y H, Clark S J, Leung C L A, Sinclair L, Marussi S, Olbinado M P, Boller E, Rack A, Todd I and Lee P D 2020 In-situ Synchrotron imaging of keyhole mode multi-layer laser powder bed fusion additive manufacturing *Appl. Mater. Today* **20** 100650
 - [31] Huang Y Z, Fleming T G, Clark S J, Marussi S, Fezzaa K, Thiyagalingam J, Leung C L A and Lee P D 2022 Keyhole fluctuation and pore formation mechanisms during laser powder bed fusion additive manufacturing *Nat. Commun.* **13** 1170
 - [32] Leung C L A, Marussi S, Towrie M, Del Val Garcia J, Atwood R C, Bodey A J, Jones J R, Withers P J and Lee P D 2018 Laser-matter interactions in additive manufacturing of stainless steel SS316L and 13–93 bioactive glass revealed by *in situ* x-ray imaging *Addit. Manuf.* **24** 647–57
 - [33] Guo Q L, Zhao C, Escano L I, Young Z, Xiong L H, Fezzaa K, Everhart W, Brown B, Sun T and Chen L Y 2018 Transient dynamics of powder spattering in laser powder bed fusion additive manufacturing process revealed by in-situ high-speed high-energy x-ray imaging *Acta Mater.* **151** 169–80
 - [34] Rees D T, Leung C L A, Elambasseril J, Marussi S, Shah S, Marathe S, Brandt M, Easton M and Lee P D 2023 *In situ* x-ray imaging of hot cracking and porosity during LPBF of Al-2139 with TiB₂ additions and varied process parameters *Mater. Des.* **231** 112031
 - [35] Bitharas I, Parab N, Zhao C, Sun T, Rollett A D and Moore A J 2022 The interplay between vapour, liquid, and solid phases in laser powder bed fusion *Nat. Commun.* **13** 2959

- [36] Sinclair L, Leung C L A, Marussi S, Clark S J, Chen Y H, Olbinado M P, Rack A, Gardy J, Baxter G J and Lee P D 2020 *In situ* radiographic and *ex situ* tomographic analysis of pore interactions during multilayer builds in laser powder bed fusion *Addit. Manuf.* **36** 101512
- [37] Weitkamp T, Tafforeau P, Boller E, Cloetens P, Valade J P, Bernard P, Peyrin F, Ludwig W, Helfen L and Baruchel J 2010 Status and evolution of the ESRF beamline ID19 *AIP Conf. Proc.* **1221** 33–38
- [38] Bhatt A, Huang Y Z, Leung C L A, Soundarapandiyam G, Marussi S, Shah S, Atwood R C, Fitzpatrick M E, Tiwari M K and Lee P D 2023 *In situ* characterisation of surface roughness and its amplification during multilayer single-track laser powder bed fusion additive manufacturing *Addit. Manuf.* **77** 103809
- [39] Schindelin J et al 2012 Fiji: an open-source platform for biological-image analysis *Nat. Methods* **9** 676–82
- [40] Leung C L A, Marussi S, Atwood R C, Towrie M, Withers P J and Lee P D 2018 *In situ* x-ray imaging of defect and molten pool dynamics in laser additive manufacturing *Nat. Commun.* **9** 1355
- [41] Tinevez J Y, Perry N, Schindelin J, Hoopes G M, Reynolds G D, Laplantine E, Bednarek S Y, Shorte S L and Eliceiri K W 2017 TrackMate: an open and extensible platform for single-particle tracking *Methods* **115** 80–90
- [42] Mills K C, Keene B J, Brooks R F and Shirali A 1998 Marangoni effects in welding *Phil. Trans. Roy. Soc. A* **356** 911–25
- [43] Leung C L A, Luczyniec D, Guo E Y, Marussi S, Atwood R C, Meisnar M, Saunders B and Lee P D 2022 Quantification of interdependent dynamics during laser additive manufacturing using x-ray imaging informed multi-physics and multiphase simulation *Adv. Sci.* **9** 2203546
- [44] Thomson W 1871 XLVI. Hydrokinetic solutions and observations *London, Edinburgh Dublin Phil. Mag. J. Sci.* **42** 362–77
- [45] Helmholtz P 1868 XLIII. On discontinuous movements of fluids *London, Edinburgh Dublin Phil. Mag. J. Sci.* **36** 337–46
- [46] Ladani L, Romano J, Brindley W and Burlatsky S 2017 Effective liquid conductivity for improved simulation of thermal transport in laser beam melting powder bed technology *Addit. Manuf.* **14** 13–23
- [47] Liu J G and Wen P 2022 Metal vaporization and its influence during laser powder bed fusion process *Mater. Des.* **215** 110505
- [48] King W E, Barth H D, Castillo V M, Gallegos G F, Gibbs J W, Hahn D E, Kamath C and Rubenchik A M 2014 Observation of keyhole-mode laser melting in laser powder-bed fusion additive manufacturing *J. Mater. Process. Technol.* **214** 2915–25
- [49] Brandau B, Da Silva A, Wilsnack C, Brueckner F and Kaplan A F H 2022 Absorbance study of powder conditions for laser additive manufacturing *Mater. Des.* **216** 110591
- [50] Leitner M, Leitner T, Schmon A, Aziz K and Pottlacher G 2017 Thermophysical properties of liquid aluminum *Metall. Mater. Trans. A* **48** 3036–45
- [51] Mayi Y A, Dal M, Peyre P, Bellet M, Metton C, Moriconi C and Fabbro R 2020 Laser-induced plume investigated by finite element modelling and scaling of particle entrainment in laser powder bed fusion *J. Phys. D: Appl. Phys.* **53** 075306
- [52] Matthews M J, Guss G, Khairallah S A, Rubenchik A M, Depond P J and King W E 2016 Denudation of metal powder layers in laser powder bed fusion processes *Acta Mater.* **114** 33–42
- [53] Ashkin A 1970 Acceleration and trapping of particles by radiation pressure *Phys. Rev. Lett.* **24** 156–9
- [54] Williams M D 1982 Laser reflection from oxide-coated aluminum *Appl. Opt.* **21** 747–50
- [55] Brandl E, Heckenberger U, Holzinger V and Buchbinder D 2012 Additive manufactured AlSi10Mg samples using selective laser melting (SLM): microstructure, high cycle fatigue, and fracture behavior *Mater. Des.* **34** 159–69
- [56] SA K et al 2020 Controlling interdependent meso-nanosecond dynamics and defect generation in metal 3D printing *Science* **368** 660–5